

Timing and Spectral Study of AX J1745.6–2901 with Suzaku

Yoshiaki HYODO,¹ Yoshihiro UEDA,² Takayuki YUASA,³
Yoshitomo MAEDA,⁴ Kazuo MAKISHIMA,³ and Katsuji KOYAMA,¹

¹*Department of Physics, Graduate School of Science, Kyoto University,
Kita-shirakawa Oiwake-cho, Sakyo, Kyoto 606-8502*

²*Department of Astronomy, Graduate School of Science, Kyoto University,
Kita-shirakawa Oiwake-cho, Sakyo, Kyoto 606-8502*

³*Department of Physics, School of Science, the University of Tokyo, 7-3-1, Hongo, Bunkyo, Tokyo 113-0033*

⁴*Institute of Space and Astronautical Science, 3-1-1, Yoshinodai, Sagami-hara, Kanagawa, 229-8510
hyodo@cr.scphys.kyoto-u.ac.jp*

(Received 2008 July 12; accepted 2008 August 31)

Abstract

The eclipsing low-mass X-ray binary AX J1745.6–2901 was observed with Suzaku in its outburst phase. Combining the Chandra observation made 1.5 month earlier than Suzaku, the orbital period is determined to be 30063.76 ± 0.14 s. We found deep flux dips prior to the eclipse phase of orbit. The X-ray spectrum in the persistent phase is described with a combination of a direct and a scattered-in by dust emissions. During the eclipse, the X-ray spectrum becomes only the dust scattering (scattered-in) component. The direct component is composed of a disk-blackbody and a blackbody (neutron star surface). No power-law component is found in the hard energy band up to 30 keV. The optical depth of the dust-scattering is ~ 10.5 at 1 keV. A clear edge at ~ 7.1 keV in the deep dip spectrum indicates that the major portion of Fe in the absorber is neutral or at low ionization state. We discovered four narrow absorption lines near the K-shell transition energies of Fe XXV, Fe XXVI, and Ni XXVII. The absorption line features are well explained by the solar abundance gas in a bulk motion of $\sim 10^3$ km s⁻¹.

Key words: Galaxy: center — ISM: dust — X-rays: individual (AX J1745.6–2901) — X-rays: binaries

1. Introduction

A number of high inclination (i.e. close to edge-on) low-mass X-ray binaries (LMXB) show regular and irregular flux decrease that occurs at every orbital cycle. The former is eclipse of a central compact source by a companion low-mass star and the latter, called as "dip" is thought to obscuration by thickened outer region of accretion disk where accretion stream from the companion star impacts (White & Holt 1982). Another feature responsible for the gas near a neutron star is narrow absorption line from highly ionized ions.

The spectral changes during dip are complicated, and cannot be reproduced with simple absorption with neutral materials. Two component model consisting a compact blackbody and an extended power-law has been succeeded in explaining the dip and persistent spectra (Parmar et al. 1986; Church & Bałucińska-Church 1995; Church et al. 1997). The compact source is heavily absorbed during the dip, while the extended component is gradually absorbed as increasing dip flux. Based on the two-component model, Boirin et al. (2005) and Díaz Trigo et al. (2006) proposed an alternative interpretation that the spectra are simply explained with ionized absorber using the updated photo-ionization code.

Narrow absorption lines have been also used to diagnose the gas property surrounding a compact object, such as the abundances, ionization states, the photo-

ionization parameters or plasma temperatures of the gas. Accordingly, an X-ray source that exhibits the eclipse, dips and absorption lines is unique and powerful to study the high inclination LMXB systems. However only two LMXBs, MXB 1659–298 and EXO 0748–676 (Sidoli et al. 2001, Parmar et al. 1986), has been known to show both the eclipse and dip. Among them, MXB 1659–298 is unique showing narrow absorption lines from highly ionized atoms. The profiles of the narrow lines in MXB 1659–298 is consistent with resonance scattering by photo-ionized plasma, but shows no dependence on the dip and persistent flux.

AX J1745.6–2901 was discovered in the ASCA observations of the Galactic center (Maeda et al. 1996; Kennea & Skinner 1996). Showing a type-I X-ray burst and eclipses, it was classified as an eclipsing LMXB at a distance of ~ 10 kpc. Except the X-ray burst and eclipses, the light curve was nearly constant (Maeda 1998). The X-ray spectrum during the persistent state was featureless, and reproduced by highly absorbed ($N_{\text{H}} \sim 2.5 \times 10^{23}$ cm⁻²) power-law with a photon index of ~ 2.4 , or thermal bremsstrahlung with a temperature of ~ 7.4 keV. The orbital period derived from the periodic eclipse was 8.356 ± 0.008 hr (Maeda et al. 1996).

We discovered deep dips and narrow absorption lines from AX J1745.6–2901 with the Suzaku observations. Thus AX J1745.6–2901 is the second LMXB that exhibits the eclipse, dips and absorption lines. Furthermore,

Table 1. Observation log.

Start Date	Observatory	Obs. ID	Aim point (J2000.0)		t_{exp}^{\dagger} (ks)
			R.A.	Decl.	
2005-09-23*	Suzaku	100027010	17 ^h 46 ^m 04 ^s	-28°55'36''	49
2005-09-30*	Suzaku	100037040	17 ^h 46 ^m 04 ^s	-28°55'36''	47
2007-07-19	Chandra	8567	17 ^h 47 ^m 22 ^s	-28°11'36''	20
2007-09-03	Suzaku	102013010	17 ^h 46 ^m 03 ^s	-28°55'40''	58

* Observations used to construct the background.

† Exposure time after removing periods with high background level. Those of XIS are shown for Suzaku observations.

Suzaku provides us with the best-quality X-ray spectra in the three phases (persistent, dip, and eclipse). This paper reports a unified spectral analysis of the three phases in the combination of the narrow line analysis, and then presents a new view of the high inclination LMXB.

2. Observation and Data Reduction

The Suzaku satellite (Mitsuda et al. 2007) has carried out three observations of a field containing the Galactic nucleus Sgr A* in 2005 September, 2006 September, and 2007 September. In the observation conducted on 2007 September 3–5, AX J1745.6–2901 was detected in outburst. The observation log is given in table 1.

Suzaku has X-ray Imaging Spectrometer (XIS: Koyama et al. 2007a), consisting four X-ray CCD cameras each placed on the focal planes of the X-Ray Telescope (XRT: Serlemitsos et al. 2007). All four XRT modules are co-aligned to image the same region of 18'×18' with a half power diameter of 1'9–2'3. Three of the cameras (XIS 0, XIS 2, and XIS 3) have front-illuminated (FI) CCDs sensitive in the 0.4–12 keV energy band and the remaining one (XIS 1) has back-illuminated (BI) CCD sensitive in the 0.2–12 keV energy band. XIS 2 has been dysfunctional due to an anomaly occurred in 2006 November. Combined with XRT, the total effective area is $\sim 400 \text{ cm}^2$ at 8 keV. To mitigate the energy resolution degradation caused by charged particle radiation, the XIS has been equipped with Spaced-row Charge Injection (SCI). The details of this capability are described in Bautz et al. (2004); Bautz et al. (2007); Uchiyama et al. (2007). The SCI technique was used in the observation of 2007 September. We checked the energy scale and resolution using the Mn K α line from the calibration sources (^{55}Fe) illuminating two corners of each CCD. As a result, we confirmed that the uncertainty of absolute energy scales are less than 5 eV and the energy resolutions in the full width at half maximum (FWHM) at 5.9 keV are $\sim 145 \text{ eV}$ and $\sim 180 \text{ eV}$ for FI and BI CCDs, respectively.

Suzaku also has a non-imaging Hard X-ray Detector (HXD: Kokubun et al. 2007; Takahashi et al. 2007). The HXD is comprised of Si PIN diodes (PIN) sensitive in 10–60 keV and GSO scintillator (GSO) sensitive in 40–600 keV, both located inside an active BGO shield. The PIN has a field of view (FOV) of 34'×34' with lowest non-X-ray background ever achieved. We use only XIS

and PIN data in this paper, because AX J1745.6–2901 is below the detection limit of GSO.

The XIS and PIN data were processed with version 2.1. We removed data taken during the South Atlantic Anomaly passages and at earth elevation angles below 4°. For PIN data, we further excluded the events taken with cutoff rigidity less than 8 GV. We corrected for the dead time ($\sim 5\text{--}7\%$) of the HXD using `hxdtdcor`. The net exposure time after this filtering is $\sim 58 \text{ ks}$ for the XIS and $\sim 42 \text{ ks}$ for the PIN.

We also retrieved archived Chandra (Weisskopf et al. 2002) data to study temporal behavior of AX J1745.6–2901. We found an observation using the Advanced CCD Imaging Spectrometer (ACIS: Garmire et al. 2003) covers a field containing AX J1745.6–2901 in outburst a month and half prior to the Suzaku observation (table 1). For both Suzaku and Chandra data, barycentric corrections were applied.

3. Analysis and Results

3.1. Light curve

AX J1745.6–2901 is only $\sim 1'5$ away from Sgr A*. Since the bright supernova remnant Sgr A East (Maeda et al. 2002) contaminates to the source region and both the Galactic center diffuse X-ray emission and point source population are strongly peaked at the Galactic center (Koyama et al. 1989; Munro et al. 2003; Koyama et al. 2007b), the background photons cannot be accumulated from the nearby regions. Instead, we extracted them with the same region observed in 2005 September when the source was not in outburst. We simulated a point source image at the source position using `xissim` (Ishisaki et al. 2007), and extracted source photons at various enclosed photon fractions. Consequently, we found that a 48% enclosed photon polygon maximize the signal-to-noise ratio. For the ACIS data, source photons were extracted from a 20''×40'' elliptical region.

Figure 1 shows the ACIS and XIS light curves of AX J1745.6–2901 in the 3.0–10.0 keV energy band. The X-ray flux of AX J1745.6–2901 was highly variable; we found four type-I X-ray bursts, three fast flux drops, and two flux rises, which were already found by Maeda et al. (1996). The presence of type-I bursts confirm that AX J1745.6–2901 is an LMXB. The flux drops and rises are due to the eclipse of a companion star. We refer to the ingress times as T_1 , T_2 , and T_3 (figure 1). Because

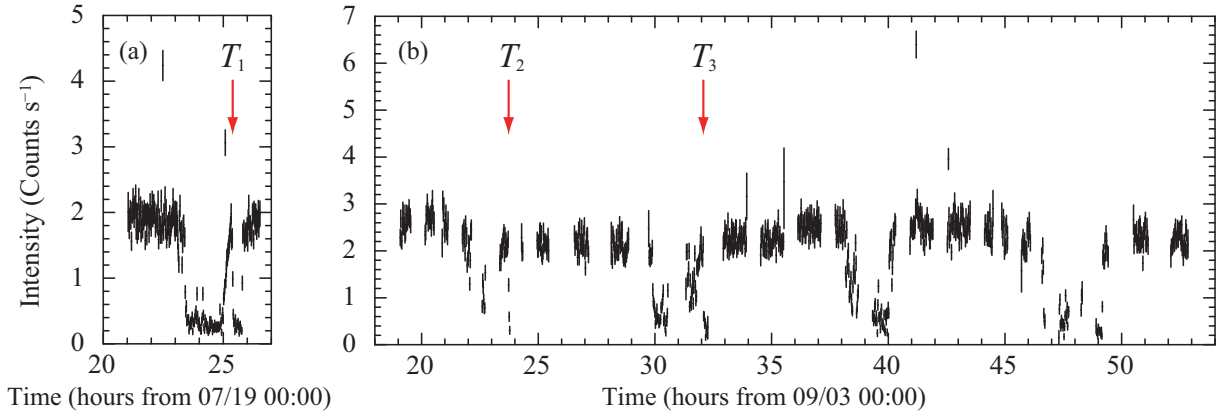


Fig. 1. Light curve of AX J1745.6–2901 in the 3.0–10.0 keV energy band with a bin time of 80 s. The red arrows indicate the eclipse ingresses. Data jumps are due to type-I X-ray bursts. (a) ACIS light curve, where background is NOT subtracted. (b) XIS light curve of combined data from the three XIS cameras, where background is subtracted.

the eclipse is expected to occur at every orbit with constant phase and duration, we assume that $T_2 - T_1 = nP_{\text{orb}}$ and $T_3 - T_2 = P_{\text{orb}}$, where n is a natural number and P_{orb} is the orbital period. Under this condition, we obtained $P_{\text{orb}} = 30063.76 \pm 0.14$ s (8.35104 ± 0.00004 hour). Figure 2 (a) shows the light curve folded with the orbital period and (b) shows the hardness ratio (counts in the 5–10 keV energy band divided by those in the 3–5 keV energy band). The phase origin point is so defined that the center of eclipse is 0.5. In addition to the above mentioned variability, we found relatively slow intensity dips in prior to the eclipses for the first time.

We here define three states of AX J1745.6–2901: “persistent” with orbital phase of 0–0.193 and 0.524–1, “dip” with orbital phase of 0.193–0.476, “eclipse” with orbital phase of 0.476–0.524 (figure 2a). The spectrum in the eclipse phase is softer, while that in the dip phase is harder on average than that in the persistent phase.

3.2. Persistent and Eclipse spectra

In the spectral analysis, we concentrate on the Suzaku data having a better energy resolution and statistics than those of Chandra. The ancillary response files (ARFs) and response matrix files (RMFs) were produced using `xissimarfgen` (Ishisaki et al. 2007) and `xisrmfgen`. Since FI CCDs have almost the same ARFs and RMFs, the XIS0 and XIS3 data were summed and simultaneously fitted with the XIS1 spectrum.

Maeda et al. (1996) reported that the X-ray spectrum during the eclipse is interpreted as the dust-scattering; a portion of X-rays emitted from the source in small off-set angle from the line of sight are scattered by the interstellar dust into the line of the source sight. We here call as the “scattered-in” component. On the other hand, vice-versa scattering process should exist; a portion of X-rays in the line of sight is “scattered-out” of the line of the source sight. We therefore fitted the persistent and eclipse spectra simultaneously as below.

$$\begin{aligned} & [\alpha \cdot e^{-\tau(E)} + \beta(E) \cdot \{1 - e^{-\tau(E)}\}] \cdot F(E) & : \text{Persistent} \\ & \beta(E) \cdot \{1 - e^{-\tau(E)}\} \cdot F(E) & : \text{Eclipse} \end{aligned}$$

, where E is the photon energy in keV, $\alpha \equiv 0.48$ is the flux ratio coming in the source region (section 3.1), and $\beta(E)$ is the fraction of the extended (dust scattering) halo coming into the source region. Unlike α , $\beta(E)$ depends on the X-ray energy (E). $\tau(E)$ is the dust-scattering optical depth, and $F(E)$ is the source spectrum. For $\tau(E)$, we assumed that the scattering optical depth is proportional to the inverse square of the photon energy, i.e., $\tau(E) = \tau_{1\text{keV}} \cdot E^{-2}$, where $\tau_{1\text{keV}}$ is the scattering optical depth at 1 keV. The first term of the persistent flux (upper equation) indicates that lower energy photons are scattered-out more than higher energy photons. The second term is scattered-in photons.

In order to estimate $\beta(E)$, we modeled the dust-scattered halo size of AX J1745.6–2901 using another X-ray binary near the Galactic center GS 1741.2–2859/1741.6–2849 as follows: (1) Mitsuda et al. (1990) measured the energy-dependent size of the dust scattering halo of GS 1741.2–2859/1741.6–2849 using the lunar occultation. Assuming that the halo size is proportional to the inverse of the photon energy, we made the two-dimensional halo extensions with an energy step of 0.25 keV. (2) We convolved the halo images with response of the XRT+XIS using `xissim` at each energy step. (3) Extracting the photons from the source region in the simulated images, we obtained the energy-dependent enclosed photon fractions and fitted with a cubic function. (4) We implemented the explicit form as $\beta(E) = (-0.02259 + 0.03046 \times E + 0.00145 \times E^2 - 0.00016 \times E^3)$ to XSPEC.

For $F(E)$, we used the standard model of low-mass binary: disk-blackbody (DBB) plus blackbody (Mitsuda et al. 1984; Makishima et al. 1986) both attenuated by a common interstellar extinction (Morrison & McCammon 1983) with solar abundances (Anders & Grevesse 1989). This simple model however was rejected with $\chi^2/\text{d.o.f.}$ (degree of freedom) = 556.0/335 (figure 3). The large χ^2 value is mainly attributed to narrow negative resid-

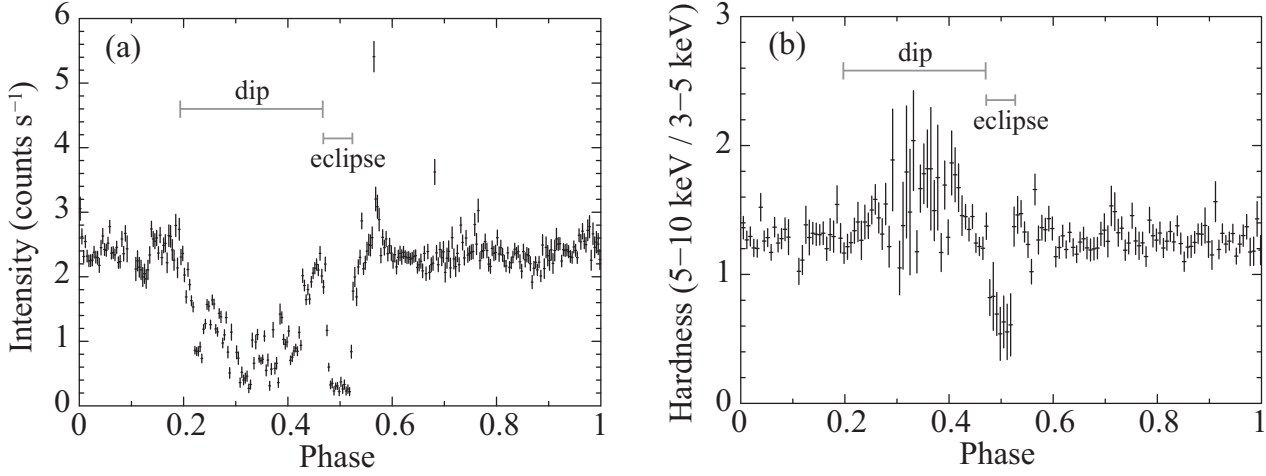


Fig. 2. (a) XIS 3–10 keV light curve folded with the orbital period of 30063.76 s. Data jumps are due to type I X-ray bursts. (b) Hardness ratio (counts in the 5–10 keV band divided by counts in the 3–5 keV band) of the folded light curve. In both panels, the background is subtracted.

uals around 6.6–8.3 keV. Adding four negative Gaussian lines to the model, we obtained an acceptable fit with $\chi^2/\text{d.o.f.} = 337.4/327$. The widths of lines were consistent with zero, and the 95% upper limit is 40 eV for 1σ in the 6.7 keV line. Allowing the iron abundance (Z_{Fe}) in the interstellar absorber to be free, we obtained a better fit with $\chi^2/\text{d.o.f.} = 310.4/326$. The best-fit parameters are shown in table 2.

The best-fit line center energies, ~ 6.69 keV, ~ 6.97 keV, ~ 7.87 keV, and ~ 8.19 keV indicate that these are due to resonance scattering by highly ionized iron and/or nickel as seen in other LMXBs (Ueda et al. 2001; Sidoli et al. 2001; Parmar et al. 2002; Boirin & Parmar 2003; Boirin et al. 2004; Boirin et al. 2005; Church et al. 2005).

We confirmed that any line is significant based on F -test. For example, even ~ 8.19 keV, having the worst statistics among the four lines, is significant at more than 99.99% confidence level with an F -value of 9.66. Fe XXV and Fe XXVI absorption edges at 8.828 keV and 9.278 keV should be accompanied with the highly ionized iron absorption lines. Then, adding edge model of XSPEC, we obtained an upper limit of ~ 0.1 for the optical depths at around 9 keV.

3.3. Dip spectra

To investigate the spectral shape and its variation during the dip, we divided the dip into two phases: “shallow dip” with the XIS count rates more than 0.7 counts s^{-1} and “deep dip” with those less than 0.7 counts s^{-1} . We first simply assume that the dip spectra are comprised of the scattered and direct components, and the latter is partially absorbed by cold matter. We fitted the spectra with the form,

$$\{\alpha \cdot PC(E) \cdot e^{-\tau(E)} + \beta(E) \cdot (1 - e^{-\tau(E)})\} \cdot F(E).$$

Here $PC(E)$ is a partial covering model given as,

$$PC(E) = f \cdot e^{-N_{\text{H}} \cdot \sigma(E)} + (1 - f),$$

Table 2. The best-fit parameters of the persistent and eclipse emission.

Component	Parameter(Unit)	Value*
Continuum		
Dust-scatter	$\tau_{1\text{keV}}$	$10.5_{-0.8}^{+0.4}$
Absorption	N_{H} (10^{23} cm^{-2})	1.87 ± 0.02
	Z_{Fe} (solar)	$1.26_{-0.16}^{+0.18}$
DBB	kT_{in}^{\dagger} (keV)	0.72 ± 0.06
	$R_{\text{in}}^2 \cos i$ (km^2) ‡	230 ± 5
Blackbody	kT (keV)	$1.64_{-0.06}^{+0.05}$
	Area (km^2) ‡	4.02 ± 0.04
Absorption lines		
Line 1	Line center (eV)	6690_{-17}^{+15}
	EW (eV)	-49_{-6}^{+7}
Line 2	Line center (eV)	6969_{-11}^{+14}
	EW (eV)	-57 ± 7
Line 3	Line center (eV)	7866_{-54}^{+57}
	EW (eV)	-31_{-12}^{+13}
Line 4	Line center (eV)	8192_{-45}^{+44}
	EW (eV)	-36_{-15}^{+14}
$F_{\text{X,persistent}}^{\S}$	($10^{-11} \text{ erg s}^{-1} \text{ cm}^{-2}$)	12
$F_{\text{X,eclipse}}^{\S}$	($10^{-11} \text{ erg s}^{-1} \text{ cm}^{-2}$)	1.3
$\chi^2/\text{d.o.f.}$		310.4/326

* The errors are at 90% confidence level.

† Temperature at the innermost radius.

‡ A distance of 10 kpc is assumed.

§ Observed energy flux in the 3.0–10.0 keV band.

$^{\parallel}$ Extinction-corrected luminosity in the 3.0–10.0 keV band.

where f is the covering fraction ($0 \leq f \leq 1$), and $\sigma(E)$ is the cross section of the absorbing material. All the parameters included in $F(E)$ were fixed to those of the best-fit values in the eclipse and persistent phase (see section 3.2).

We further examined the upper limit of ionization state of the partial covering absorber. We used `absori` model

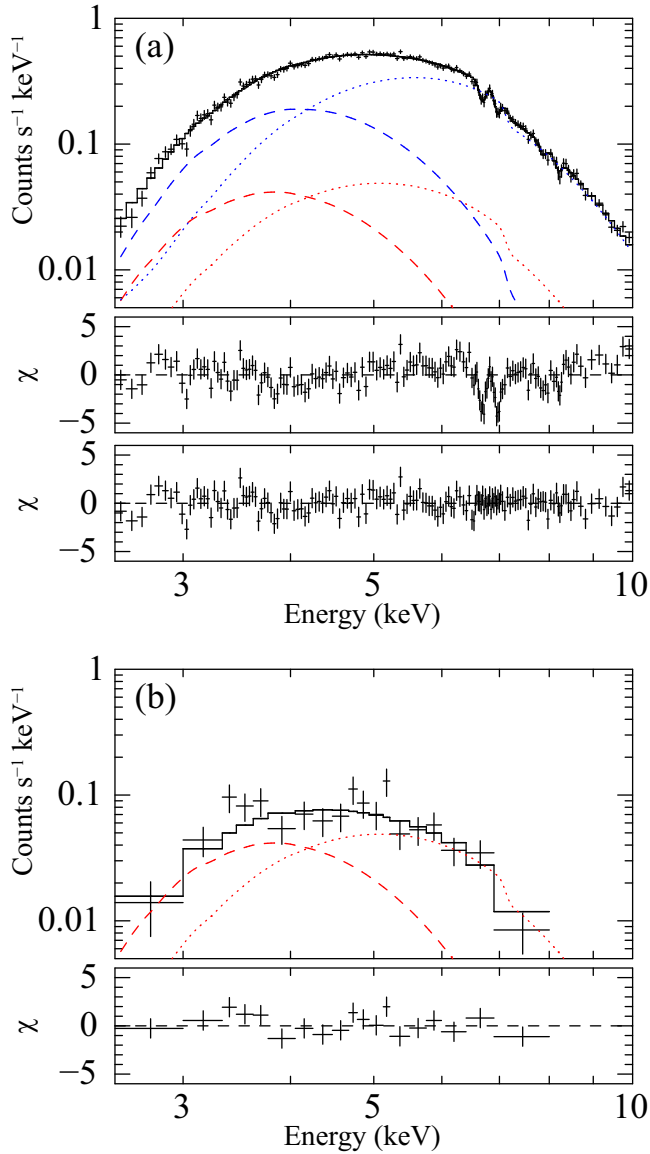


Fig. 3. (a) Background-subtracted spectrum of the persistent phase @@@ in the 2.5–10.0 keV band. Only the summed FI spectrum is shown for brevity. The top panel shows the data in crosses, the best-fit model with negative Gaussians in solid lines, the disk-blackbody in dashed lines, @@@ the blackbody in dotted lines, the scattered component in red and direct components in blue, respectively. The middle and bottom panels show the residuals between data and the best-fit model without and with Gaussians. (b) Same as (a), but of the eclipse state.

(Done et al. 1992; Magdziarz & Zdziarski 1995) in XSPEC and found that the 90% upper limit of ionization parameter $\xi (= \frac{L}{nr^2})$ is 4.7 and 0.03 for the shallow and deep dip states, respectively. Alternatively, we fixed the iron abundance in the absorber to 0 and added absorption edge. Then we obtained the edge energy, $7.25^{+0.19}_{-0.12}$ keV and $7.16^{+0.08}_{-0.07}$ keV in the shallow and deep dip state respectively.

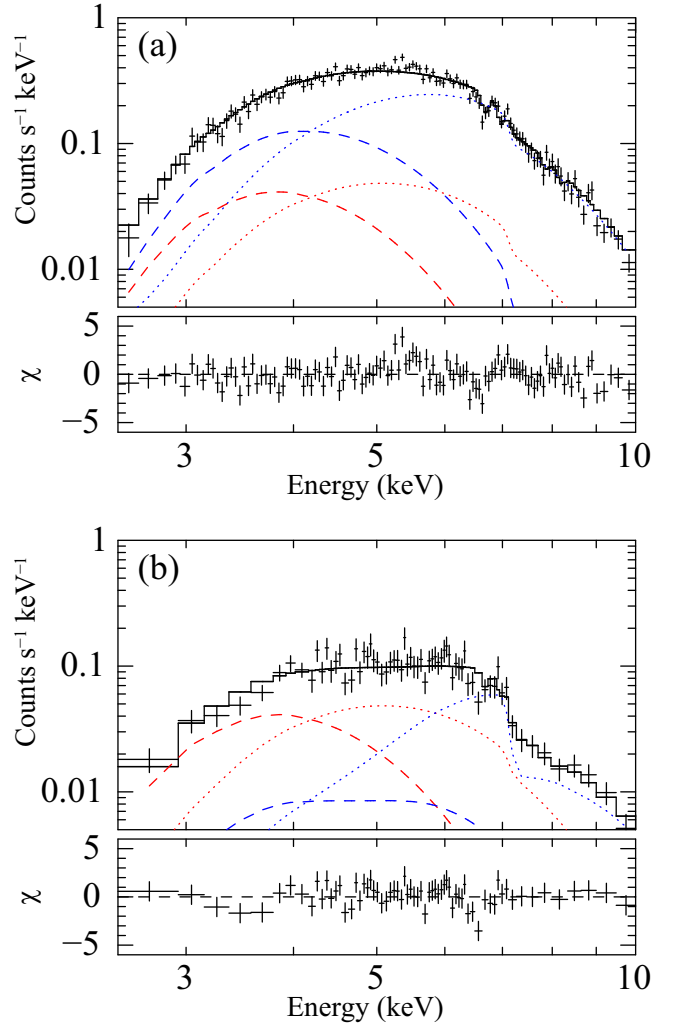


Fig. 4. (a) Same as figure 3, but for the shallow dip state. (b) Same as figure 3, but for the deep dip state.

Table 3. The best-fit parameters of the dip state with a cold partial covering absorber model.

Parameter (Unit)	Value*	
	Shallow dip	Deep dip
f	0.35 ± 0.03	0.96 ± 0.01
N_{H} (10^{23} cm $^{-2}$)	$6.1^{+1.8}_{-1.2}$	$10.4^{+0.9}_{-0.8}$
F_{X} (10^{-11} erg s $^{-1}$ cm $^{-2}$)	9.1	2.8
$\chi^2/\text{d.o.f.}$	264.9/225	95.6/89

* The errors are at 90% confidence level.

3.4. XIS+HXD analysis

AX J1745.6–2901 is in the high background area of the Galactic centre diffuse X-ray (GCDX) (Koyama et al. 1996; Koyama et al. 2007b; Yuasa et al. 2008). Also transient or time variable sources may be in the PIN FOV. To avoid systematic errors due to the GCDX and transient/time variable sources, we made a “difference-spectrum” of PIN. We first excluded the non-X-ray back-

Table 4. The best-fit parameters for the "difference spectrum" (persistent minus eclipse spectra) of the combined spectra of XIS and HXD.

Component	Parameter (Unit)	Value*
Absorption	N_{H} (10^{23} cm $^{-2}$)	$1.72^{+0.06}_{-0.05}$
	Z_{Fe} (solar)	1.32 ± 0.18
DBB	kT_{in} (keV)	0.70 ± 0.07
	$R_{\text{in}}^2 \cos i$ (km 2)	190 ± 20
Blackbody	kT (keV)	1.64 ± 0.07
	Area (km 2)	4.14 ± 0.04
F_{X}	(10^{-11} erg s $^{-1}$ cm $^{-2}$)	11
$\chi^2/\text{d.o.f.}$		150.8/150

* The errors are at 90% confidence level.

† Absorption-corrected luminosity in the 3 – 10 keV band. A distance of 10 kpc is assumed.

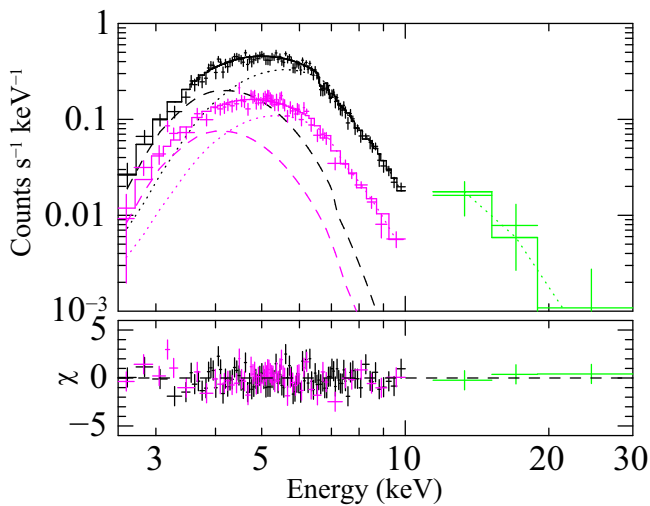


Fig. 5. Same as figure 3, but the background is extracted from the eclipse state. Top panel shows the summed FI data in black, the BI data in magenta, and the HXD data in green.

ground (NXB) signals of the PIN from the persistent and eclipse state respectively, and subtracted the NXB-excluded eclipse spectrum from the NXB-excluded persistent spectrum.

Since AX J1745.6–2901 resides apart from the optical axis of the HXD by $\sim 7'$ in the present observation attitude, the effective area of PIN decreases by $\sim 20\%$. We calculated the corresponding ARF using `hxdarfgen`, and applied it in the spectral analysis. Making the XIS spectrum in the same way, we performed the simultaneous fitting to the XIS and HXD data. We fixed the PIN/XIS cross-normalization factor to 1.15, the mean value of luminous sources (Kokubun et al. 2007; Reeves et al. 2007; Miniutti et al. 2007; Shirai et al. 2008; Markowitz et al. 2008).

The scattered-in component should be automatically subtracted in this method, and hence only the direct component is taken into account. Since the photon statistics is limited, the absorption line parameters and $\tau_{\text{rm}1\text{keV}}$, responsible for scattering-out, are fixed to those derived

in §3.2. The XIS and HXD spectra are well reproduced by almost the same parameters in the direct component in §3.2 (figure 5). As is seen in figure 5, the hard band data (~ 10 –30 keV) is simply described by the blackbody spectrum of $kT = 1.64 \pm 0.07$ keV, which is most likely due to the emission of a neutron star surface. No hard tail (power-law) component such as the Compton-up scattering emission is required.

4. Discussion

4.1. Persistent Spectra

AX J1745.6–2901 is the second low-mass X-ray binary that exhibits dips, eclipse and X-ray burst, and absorption lines. Using the best-quality Suzaku spectra of AX J1745.6–2901, we found a clearer picture of this LMXB type. The X-ray spectrum in the persistent phases are described with a combination of direct, and dust scattering (scattered-in and scattered-out) emissions. The direct component is composed of DBB and a blackbody (neutron star surface). Although dipping/eclipsing sources are high inclination (nearly disk-edge on) systems, we need no power-law components in the hard energy band up to 30 keV, and hence Compton-up scattering by possible hot disk corona is absent (see section 4.3).

4.2. Eclipse Spectra

The eclipse spectrum is purely dust scattering (scattered-in) component with a large optical depth ($\tau_{1\text{keV}}$) of 10. Predehl & Schmitt (1995) conducted a systematic study on interstellar absorption and dust scattering using the ROSAT data. They found $\tau_{1\text{keV}}$ and N_{H} correlates well with $N_{\text{H}}/\tau_{1\text{keV}} \sim 2 \times 10^{22}$ cm $^{-2}$ in the N_{H} range of 0 – 3×10^{22} cm $^{-2}$. Our data for AX J1745.6–2901 $N_{\text{H}}/\tau_{1\text{keV}} \sim 1.8 \times 10^{22}$ cm $^{-2}$ extends this relation over nearly one order of magnitude of N_{H} , up to $\sim 2 \times 10^{23}$ cm $^{-2}$. Conversely, this good correlation strongly supports our assumption that the eclipse emission is due to dust scattering. Also the gas-to-dust ratio towards the Galactic center is not largely different from the other regions in the Galaxy.

4.3. Dip Spectra

The spectra are simply explained by a partial covering model in both the deep and shallow dips. No extended emission of power-law spectrum such as Compton-up scattering is required. The flux decrease is mainly due to the increase of the covering factor, together with a slight increase of N_{H} . Unlike the prediction of Díaz Trigo et al. (2006), the absorption gas is not highly ionized. The upper limit of photo-ionization parameter $\xi (= \frac{L}{nr^2})$ is 0.03–4.7, depending on the depth of dip.

4.4. Absorption lines

We found four absorption lines with the respective line center energies and equivalent widths of (1) 6690^{+15}_{-17} eV and 49^{+7}_{-6} eV, (2) 6969^{+14}_{-11} eV and 57 ± 7 eV, (3) 7866^{+57}_{-54} eV and 31^{+13}_{-12} eV, and (4) 8192^{+44}_{-45} eV and 36^{+14}_{-15} eV. Since the absorption line features are found in every orbital phases,

these are due to disk corona gas. From the center energies of the absorption lines, we infer that (1) and (2) are Fe XXV $K\alpha$ and Fe XXVI $K\alpha$, respectively. Line (3) would be a complex of Fe XXV $K\beta$ and Ni XXVII $K\alpha$, while line (4) is Fe XXVI $K\beta$ plus Ni XXVIII $K\alpha$. The EW of resonance scattering absorption line is a function of both the column density and velocity dispersion along the line of sight (Δv_{los}), whereas the absorption edge depth of corresponding ionic species depends only on the column density. The upper limit of absorption edge ($\tau \leq 0.1$) gives upper limit of $\sim 5 \times 10^{18} \text{ cm}^{-2}$ for N_{FeXXV} . Combining the EW of the 6.7 keV line (49 eV), we constrain the lower limit of $\Delta v_{\text{los}} \geq 4 \times 10^2 \text{ km s}^{-1}$ (see figure 3 in Kotani et al. 2006). On the other hand, the upper limit of $\Delta v_{\text{los}} < 2 \times 10^3 \text{ km s}^{-1}$ is obtained from the upper limit of the line width of 40 eV.

For simplicity, we assume an intermediate value of $\Delta v_{\text{los}} = 7 \times 10^2 \text{ km s}^{-1}$ (kinematics temperature of 10² keV, figure 3 by Kotani et al. 2006), and discuss physical condition of iron and nickel by referring figure 3 of Kotani et al. (2006). Using the EWs of FeXXV and FeXXVI lines of 49 eV and 57 eV, we estimate the column density of FeXXV (N_{FeXXV}) and FeXXVI (N_{FeXXVI}) to be $1.8_{-0.6}^{+0.7} \times 10^{18} \text{ cm}^{-2}$ and $4.2_{-2.5}^{+3.6} \times 10^{18} \text{ cm}^{-2}$, respectively. Then EWs of $K\beta$ of FeXXV and FeXXVI are estimated to be $20 \pm 5 \text{ eV}$ and 17_{-6}^{+9} eV respectively, and hence EWs of $K\alpha$ of NiXXVII and NiXXVIII are $< 24 \text{ eV}$ and $19_{-15}^{+10} \text{ eV}$. The latter two values constrain N_{NiXXVII} and N_{NiXXVIII} to be $< 4 \times 10^{17} \text{ cm}^{-2}$ and $4_{-3}^{+4} \times 10^{17} \text{ cm}^{-2}$, respectively. The ionic fractions of FeXXVI and NiXXVIII are 0.68 ± 0.08 and 0.40 ± 0.05 , so the abundance ratio of Ni/Fe is $0.13_{-0.10}^{+0.13}$, which is consistent with the solar value (Anders & Grevesse 1989). Assuming the solar abundance of iron, the N_{H} value for the absorption gas is $\sim 1.3 \times 10^{23}$, or optical depth of Thomson scattering (τ_{es}) is ~ 0.1 .

The ratio of $N_{\text{FeXXVI}}/N_{\text{FeXXV}}$ gives the plasma temperature of $13 \pm 4 \text{ keV}$ in collisional equilibrium (Arnaud & Raymond 1992). On the other hand, if the absorption gas is due to photo-ionized plasma, then the ionization parameter (ξ) is $\sim 10^{3.5}$ and the plasma temperature is $\sim 100 \text{ eV}$. Using the plasma temperatures given above, the random (thermal) velocity of iron/nickel estimated to be less than 300 km s^{-1} , significantly lower than 700 km s^{-1} . Therefore the velocity of 700 km s^{-1} would be mainly attributable to a bulk motion of the gas.

This velocity is very small as an electron velocity, therefore in any case, the electron temperature is less than 20 keV, and hence the y parameter ($4\tau_{\text{es}} \cdot kT/511 \text{ keV}$) is less than 0.02. This small value of y is consistent with no Compton-up scattering flux in the hard energy band (section 4.1).

5. Summary

We observed the eclipsing LMXB AX J1745.6–2901 in an outburst phase with Suzaku. The results are summarized as follows:

1. Combining the Chandra data obtained 1.5 month

earlier than Suzaku, the orbital period is more accurately constrained than before to be $30063.76 \pm 0.14 \text{ s}$.

2. Irregular dipping activity was found for the first time.
3. Narrow absorption lines were detected at $\sim 6.7 \text{ keV}$, $\sim 6.9 \text{ keV}$, $\sim 7.8 \text{ keV}$, and $\sim 8.2 \text{ keV}$.
4. The narrow line profiles are described by absorptions of K-shell transition of highly ionized iron and nickel in solar abundance.
5. The persistent spectrum is well modeled with a direct and scattered in by dust component.
6. The eclipse spectrum is comprised only of the scattered-in component.
7. The dip spectra are well reproduced by direct emission absorbed by cold matter and the scattered-in component.
8. The HXD signal in the 12–30 keV band was detected by subtracting the eclipse spectrum from persistent spectrum. The emission was reproduced by a black-body component with a temperature of $\sim 1.6 \text{ keV}$. No significant hard tail was detected.

We thank Makoto Sawada and Taro Kotani for useful comments and discussions. Y. H. and T. Y. are financially supported by the Japan Society for the Promotion of Science. The work is financially supported by the grants-in-aid for a 21st century center of excellence program “Center for Diversity and Universality in Physics” and No. 18204015 by the Ministry of Education, Culture, Sports, Science and Technology of Japan. This research has made use of data obtained from the Data ARchive and Transmission System at ISAS/JAXA.

References

- Anders, E., & Grevesse, N. 1989, *Geochim. Cosmochim. Acta*, 53, 197
- Arnaud, M., & Raymond, J. 1992, *ApJ*, 398, 394
- Bautz, M. W., Kissel, S. E., Prigozhin, G. Y., LaMarr, B., Burke, B. E., & Gregory, J. A. 2004, *Proc. SPIE*, 5501, 111
- Bautz, M. W., *Proc. SPIE*, 6686
- Boirin, L., & Parmar, A. N. 2003, *A&A*, 407, 1079
- Boirin, L., Parmar, A. N., Barret, D., Paltani, S., & Grindlay, J. E. 2004, *A&A*, 418, 1061
- Boirin, L., Méndez, M., Díaz Trigo, M., Parmar, A. N., & Kaastra, J. S. 2005, *A&A*, 436, 195
- Church, M. J., & Bałucińska-Church, M. 1995, *A&A*, 300, 441
- Church, M. J., Dotani, T., Bałucińska-Church, M., Mitsuda, K., Takahashi, T., Inoue, H., & Yoshida, K. 1997, *ApJ*, 491, 388
- Church, M. J., Reed, D., Dotani, T., Bałucińska-Church, M., & Smale, A. P. 2005, *MNRAS*, 359, 1336
- Díaz Trigo, M., Parmar, A. N., Boirin, L., Méndez, M., & Kaastra, J. S. 2006, *A&A*, 445, 179
- Done, C., Mulchaey, J. S., Mushotzky, R. F., & Arnaud, K. A. 1992, *ApJ*, 395, 275
- Garmire, G. P., Bautz, M. W., Ford, P. G., Nousek, J. A., & Ricker, G. R., Jr. 2003, *Proc. SPIE*, 4851, 28
- Hayakawa, S. 1970, *Progress of Theoretical Physics*, 43, 1224
- Ishisaki, Y., et al. 2007, *PASJ*, 59, S113

- Jimenez-Garate, M. A., Schulz, N. S., & Marshall, H. L.
Kallman, T., & Bautista, M. 2001, *ApJS*, 133, 221
Kallman, T. R., Palmeri, P., Bautista, M. A., Mendoza, C., & Krolik, J. H. 2004, *ApJS*, 155, 675
Kennea, J. A., & Skinner, G. K. 1996, *PASJ*, 48, L117
Kokubun, M., et al. 2007, *PASJ*, 59, S53
Kotani, T., Ebisawa, K., Dotani, T., Inoue, H., Nagase, F., Tanaka, Y., & Ueda, Y. 2000, *ApJ*, 539, 413
Kotani, T., Ebisawa, K., Dotani, T., Inoue, H., Nagase, F., Tanaka, Y., & Ueda, Y. 2006, *ApJ*, 651, 615
Koyama, K., Awaki, H., Kunieda, H., Takano, S., & Tawara, Y. 1989, *Nature*, 339, 603
Koyama, K., Maeda, Y., Sonobe, T., Takeshima, T., Tanaka, Y., & Yamauchi, S. 1996, *PASJ*, 48, 249
Koyama, K., et al. 2007a, *PASJ*, 59, S23
Koyama, K., et al. 2007b, *PASJ*, 59, S245
Maeda, Y., Koyama, K., Sakano, M., Takeshima, T., & Yamauchi, S. 1996, *PASJ*, 48, 417
Maeda, Y. 1998, Ph.D. Thesis, Kyoto University
Maeda, Y., et al. 2002, *ApJ*, 570, 671
Magdziarz, P., & Zdziarski, A. A. 1995, *MNRAS*, 273, 837
Makishima, K., Maejima, Y., Mitsuda, K., Bradt, H. V., Remillard, R. A., Tuohy, I. R., Hoshi, R., & Nakagawa, M. 1986, *ApJ*, 308, 635
Markowitz, A., et al. 2008, *PASJ*, 60, 277
Mathis, J. S., & Lee, C.-W. 1991, *ApJ*, 376, 490
Miniutti, G., et al. 2007, *PASJ*, 59, 315
Mitsuda, K., et al. 1984, *PASJ*, 36, 741
Mitsuda, K., Takeshima, T., Kii, T., & Kawai, N. 1990, *ApJ*, 353, 480
Mitsuda, K., et al. 2007, *PASJ*, 59, S1
Morrison, R., & McCammon, D. 1983, *ApJ*, 270, 119
Muno, M. P., et al. 2003, *ApJ*, 589, 225
Muno, M. P., Bauer, F. E., Bandyopadhyay, R. M., & Wang, Q. D. 2006b, *ApJS*, 165, 173
Oosterbroek, T., Parmar, A. N., Sidoli, L., in't Zand, J. J. M., & Heise, J. 2001, *A&A*, 376, 532
Parmar, A. N., White, N. E., Giommi, P., & Gottwald, M. 1986, *ApJ*, 308, 199
Parmar, A. N., Oosterbroek, T., Boirin, L., & Lumb, D. 2002, *A&A*, 386, 910
Predehl, P., & Schmitt, J. H. M. M. 1995, *A&A*, 293, 889
Reeves, J. N., et al. 2007, *PASJ*, 59, 301
Sakano, M., Koyama, K., Murakami, H., Maeda, Y., & Yamauchi, S. 2002, *ApJS*, 138, 19
Serlemitsos, P., et al. 2007, *PASJ*, 59, S9
Shirai, H., et al. 2008, *PASJ*, 60, 263
Sidoli, L., Oosterbroek, T., Parmar, A. N., Lumb, D., & Erd, C. 2001, *A&A*, 379, 540
Takahashi, T., et al. 2007, *PASJ*, 59, S35
Ueda, Y., Asai, K., Yamaoka, K., Dotani, T., & Inoue, H. 2001, *ApJL*, 556, L87
Ueda, Y., Murakami, H., Yamaoka, K., Dotani, T., & Ebisawa, K. 2004, *ApJ*, 609, 325
Uchiyama, H., et al. 2007, *Proc. SPIE*, 6686,
Weisskopf, M. C., Brinkman, B., Canizares, C., Garmire, G., Murray, S., & Van Speybroeck, L. P. 2002, *PASP*, 114, 1
White, N. E., & Holt, S. S. 1982, *ApJ*, 257, 318
Yuasa, T., et al. 2008, *PASJ*, 60, 207